Materials Advances

ROYAL SOCIETY OF CHEMISTRY

PAPER

View Article Online
View Journal | View Issue

Cite this: *Mater. Adv.*, 2020, **1**, 617

High-efficiency perovskite solar cells with poly(vinylpyrrolidone)-doped SnO_2 as an electron transport layer

Meiying Zhang,[a] Fengmin Wu,[ab] Dan Chi,*[a] Keli Shi*[a] and Shihua Huang*[a]

Received 14th February 2020,
Accepted 5th June 2020

DOI: 10.1039/d0ma00028k

rsc.li/materials-advances

Hybrid organic–inorganic perovskites have attracted intensive attention as the absorber layer in high-performance perovskite solar cells (PSCs). The interface between the electron transport layer and the perovskite layer in perovskite solar cells has a large effect on the device performance. Herein, we report a perovskite solar cell with a cell structure of ITO/ETL/$(FAPbI_3)_{0.97}(MAPbBr_3)_{0.03}$/spiro-OMeTAD/$MoO_3$/Ag, where the poly(vinylpyrrolidone) (PVP)-doped SnO_2 film works as the electron transport layer. We observe that the perovskite film grown on PVP-SnO_2 shows more uniform crystalline grains than the control sample grown on the pure SnO_2, and the electron mobility of the PVP-SnO_2 film is higher than that of the pure SnO_2 film; consequently, PVP-SnO_2 can efficiently extract electrons from the perovskite layer. As a result, the PSCs using the PVP-doped SnO_2 ETL showed an increased power conversion efficiency (PCE). The optimized device using the PVP-SnO_2 electron transport layer shows an improved PCE of 19.55%, while the PSC using the SnO_2 electron transport later shows a PCE of 17.50%. Furthermore, it is feasible to add PVP into the electron transport layer of SnO_2 to improve the performance of the planar perovskite solar cell device.

Introduction

Perovskite solar cells (PSCs) with a simple planar structure have the advantages of high efficiency, low cost and facile solution processing, and have become one of the most competitive and promising next-generation photovoltaic technologies.[1–4] The power conversion efficiency (PCE) of PSCs swiftly increased from 3.8% to more than 25% in 10 years due to their high absorption coefficient and long carrier diffusion length.[5–13]

A significant amount of research effort has focused on controlling the composition and morphology of perovskites,[14] as well as exploring effective and promising materials for hole and electron transport layers (HTLs and ETLs).[15–18] Comprehensive improvements in each of these areas have led to the increased PCE records. Despite the excellent performance of PSCs, planar PSCs are normally unstable and have severe hysteresis due to ion migration and interface defects in the device.[19–21] Many research groups report that modifying the interface between the perovskite layer and the ETL can significantly eliminate the hysteresis in PSCs.[22] So far, it has been believed that an effective and promising ETL is critical to make efficient and hysteresis-free PSCs.[23] A suitable ETL should meet some of the basic requirements for high equipment efficiency,[24] including proper optical transmission of the ETL to ensure adequate light penetration into the perovskite absorber; energy level matching with the conduction band edge of the perovskite material to produce the desired open circuit voltage (V_{OC}); and a high electron mobility to effectively extract carriers from the active layer to minimize the charge accumulation at the interface and facilitate electron extraction in planar PSCs.[25–27] Therefore, developing high-quality ETLs with suitable energy levels and high electron mobility is important for high efficiency devices. SnO_2 exhibits exceptional attributes including excellent chemical stability, high electron mobility, and a facile and relatively low-temperature preparation process.[28,29] So far, SnO_2 is normally used as the ETL in high-performance perovskite solar cells due to its excellent photoelectric properties.[30] Moreover, SnO_2 is found to be a good ETL of perovskite solar cells, owing to the more matched energy level between SnO_2 and perovskites.[31,32] Ke *et al.* first used the SnO_2 ETL in conventional planar PSCs and achieved a PCE of 16.02% with no observable hysteresis.[25] So far, many methods have been developed to successfully prepare compact and pinhole-free SnO_2 films, including spin-coating, atomic layer deposition, and slot-die printing.[33,34] To further increase the PCE of PSCs, improvement of the open-circuit voltage (V_{OC}) and fill factor (FF) could be more feasible than increasing the short-circuit current (J_{SC}) because J_{SC} is

[a] *Provincial Key Laboratory of Solid State Optoelectronic Devices, Zhejiang Normal University, Jinhua 321004, China. E-mail: chidan@zjnu.edu.cn, shikeli@iccas.ac.cn, huangshihua@zjnu.cn*
[b] *School of Sciences, Zhejiang Sci-Tech University, Hangzhou 310018, China*

almost close to its limit ($\sim$26 mA cm^{-2}) for perovskite solar cells with a bandgap of around 1.55 eV.[35] With these factors in mind, research efforts should begin with finding ways to increase V_{OC}. To avoid charge accumulation at the ETL/perovskite interface, researchers developed several strategies to further increase the electron mobility of SnO_2, which facilitates electron extraction.[36] For example, the compactness and wetting property of the SnO_2 layer are significantly improved by introducing polymer polyethylene glycol (PEG) into the SnO_2 ETL, thereby improving the performance of the planar perovskite solar cell.[37] The concept of introducing a polymer into the ETL paves the way to further improve the performance of planar perovskite solar cells. As a common water-soluble polymer, poly(vinylpyrrolidone) (PVP) was successfully added into SnO_2 as an ETL and improves the performance of perovskite photodetectors. PVP can inhibit the agglomeration of SnO_2 nanoparticles and improve the morphology of SnO_2 films.[38] This work provides the idea of incorporating PVP in SnO_2 as an ETL in perovskite solar cells.

Here, we report on the use of PVP-doped SnO_2 (PVP-SnO_2) as an ETL for PSCs to increase the efficiency and reduce hysteresis compared to SnO_2-based control devices. It is also demonstrated that the ETL with the PVP-doped SnO_2 can improve the crystallinity of the perovskite and extract electrons more effectively. Therefore, the best-performance device of perovskite solar cells using PVP-SnO_2 as the ETL achieved a PCE of 19.55%, with a V_{OC} of 1.120 V, a J_{SC} of 23.83 mA cm^{-2}, and a FF of 73.27%. More importantly, the device with the PVP-SnO_2 ETL showed better stability than the control device.

Results and discussion

The device structure of the perovskite solar cells we used in this study is shown in Fig. 1a. The full device structure is ITO/ETL/$(FAPbI_3)_{0.97}(MAPbBr_3)_{0.03}$/spiro-OMeTAD/$MoO_3$/Ag, in which the SnO_2 film or PVP-SnO_2 film is the ETL for the reference and test devices, respectively.

We optimized the performance of the PVP-SnO_2-based solar cells by varying the content of PVP in the PVP-SnO_2 precursor. As the PVP content increased from 2 mg mL^{-1} to 3 mg mL^{-1}, the PCE of the corresponding PSCs was improved from 18.22% to 19.55%. When the concentration of PVP increased to 5 mg mL^{-1}, the PCE was decreased to 17.80%. The conductivity of PVP is poor, so the higher concentration of PVP in SnO_2 can damage the charge carrier mobility of the SnO_2 layer. Accordingly, excessive PVP polymer cannot improve the performance of perovskite solar cells. The *J–V* curves for the PVP-SnO_2-based devices with different PVP contents are provided in Fig. 1b, and the device performance parameters are summarized in Table 1.

Fig. 2a shows the optical transmission spectra of the bare indium tin oxide (ITO), ITO/SnO_2 and ITO/PVP-SnO_2 (3 mg mL^{-1} PVP in SnO_2 solution) films. It is found that the transmittances of the ITO/SnO_2 and ITO/PVP-SnO_2 films in the wavelength range of 300–500 nm are higher than the ITO without a coating. The ITO/PVP-SnO_2 film has the best transmittance, thereby permitting more light to be absorbed by the perovskite layer. Therefore it proves that ITO/PVP-SnO_2 has good optical quality. The introduction of SnO_2 may change the reflectance over the entire wavelength region. Hence, the transmittances of the ITO/SnO_2 and ITO/PVP-SnO_2 films in the wavelength range of 300–500 nm are higher than the ITO without a coating, while the transmittances of the ITO/SnO_2 and ITO/PVP-SnO_2 films in the wavelength range of 500–900 nm are lower than the ITO without a coating.[36] It is known that the electron mobility is a key parameter of ETLs in PSCs, so it is necessary to know the electron mobility of ETLs. The electron mobilities of different ETLs were measured using the space charge-limited current (SCLC) method,[39] as shown in Fig. 2b. It is found that the electron mobility of PVP-SnO_2 is 2.75 $\times$ 10^{-3} cm^2 V^{-1} s^{-1}, higher than that of SnO_2 (2.24 $\times$ 10^{-3} cm^2 V^{-1} s^{-1}). The high electron mobility of the PVP-SnO_2 based PSCs effectively promotes electron transfer and reduces charge accumulation at the ETL/perovskite interface, which improves the efficiency and suppresses hysteresis.[27,36]

The X-ray photoelectron spectra (XPS) of the SnO_2 and PVP-SnO_2 films deposited on ITO glass substrates were measured to confirm the existence of PVP, and the corresponding results are shown in Fig. 2c. All XPS measurements of binding energy data have been calibrated through the carbon 1s line at 284.8 eV. It is clear from these measurements that SnO_2 shows distinct

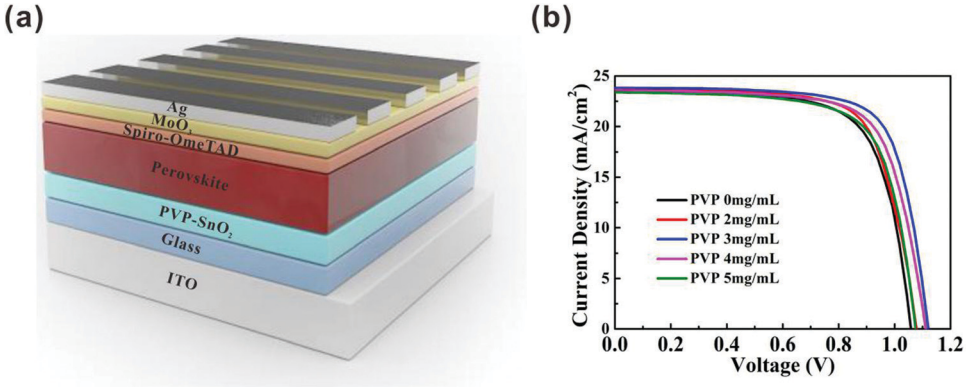

Fig. 1 (a) Schematic view of the device structure in this work. (b) *J–V* characteristics of PSCs with PVP-SnO_2 ETLs with various amounts of PVP.

Table 1 Photovoltaic performance of perovskite solar cells based on the SnO_2 ETL with various amounts of PVP

ETLs	V_{OC} (V)	J_{SC} (mA cm^{-2})	FF (%)	PCE (%)
PVP-SnO_2 (2 mg mL^{-1})	1.084	23.66	71.03	18.22
PVP-SnO_2 (3 mg mL^{-1})	1.120	23.83	73.27	19.55
PVP-SnO_2 (4 mg mL^{-1})	1.111	23.52	71.44	18.67
PVP-SnO_2 (5 mg mL^{-1})	1.074	23.40	70.76	17.80

peaks of Sn and O. After the PVP treatment, the PVP-SnO_2 film shows not only peaks of Sn and O, but also an additional peak located at 400 eV ascribed to N, which indicates the successful incorporation of PVP into SnO_2. Meanwhile, the inset gives specific XPS spectra at Sn 3d peaks of the SnO_2 and the PVP-SnO_2 films. It is obvious that the Sn 3d peak of the PVP-SnO_2 film was shifted to higher binding energy by 0.2 eV in contrast to that of the pristine SnO_2, indicating that PVP is bound to SnO_2.[36] PVP can inhibit the agglomeration of SnO_2 nanoparticles and improve the morphology of the SnO_2 film,[38] as shown in Fig. 2d. PVP can suppress the defects between the ETL layer and the perovskite and decrease the leakage current of the interface, thus improving the performance of perovskite solar cells. If the concentration of PVP is too large, the transportation of charge carriers will be damaged because of the poor conductivity of PVP. Therefore, a 2 mg mL^{-1} concentration of PVP is optimal for achieving the highest PCE and larger concentrations of PVP will inhibit the properties of perovskite solar cells.

The interface between the perovskite layer and the ETL layer has a significant effect on the device performance. Therefore, it is critical to examine the morphology of ETLs. We use atomic force microscopy (AFM) images to study the roughnesses of the pristine SnO_2 and PVP-SnO_2 films (3 mg mL^{-1} in SnO_2 solution) deposited on ITO glass substrates as shown in Fig. 3a and b. It is also found that the roughness of the PVP-SnO_2 film is higher (RMS: 3.72 nm) than that of the pristine SnO_2 film without PVP (RMS: 2.44 nm). The surface roughness of the ETL compact layer could affect electron transport as it affects the contact area between the perovskite active layers and the ETL layer.[40] An appropriately high roughness of PVP-SnO_2 could lead to an increase in the contact area between the active layer and the ETL layer, thereby leading to improved charge transport.[41,42]

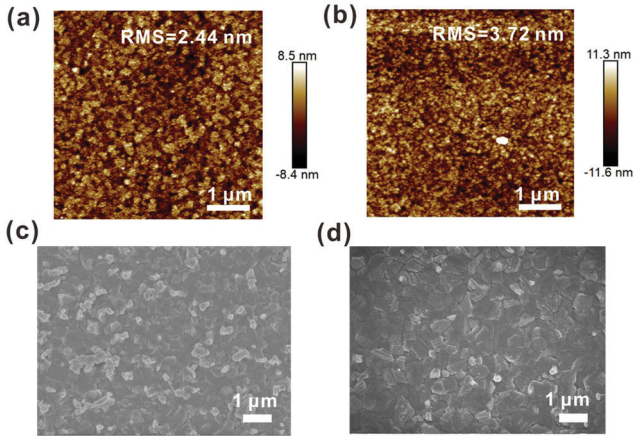

Fig. 3 AFM images of the SnO_2 (a) and the PVP-SnO_2 (b) films deposited on ITO. SEM images of the perovskites coated on the SnO_2 film (c) and the PVP-SnO_2 film (d).

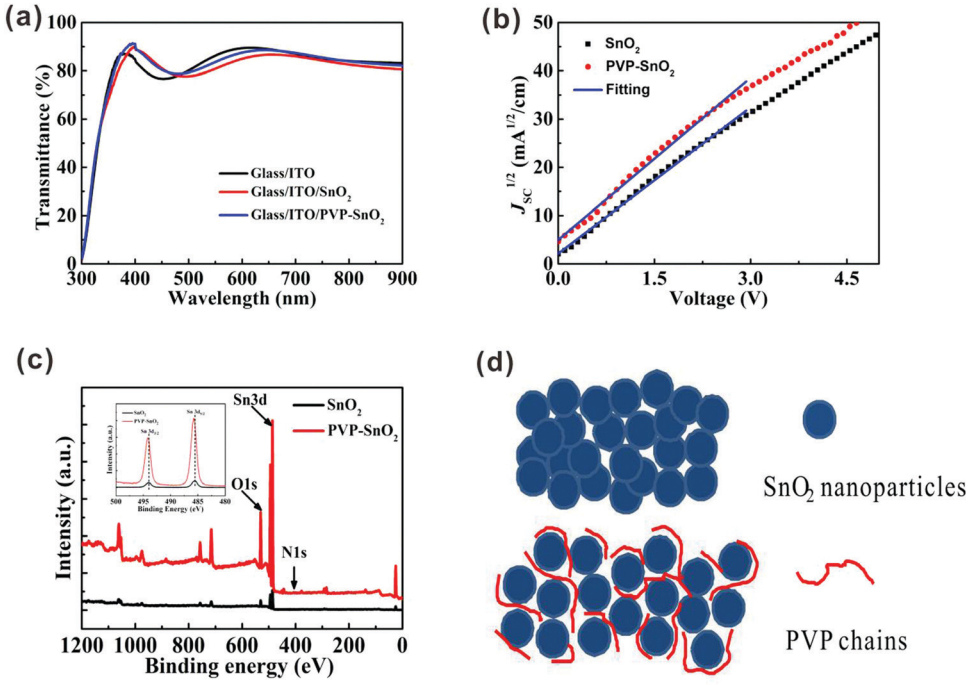

Fig. 2 (a) Transmission spectra of ITO, ITO with SnO_2, and ITO with PVP-SnO_2 substrates. (b) $J^{1/2}$–V plots for obtaining the electron mobilities of the SnO_2 and PVP-SnO_2 films using the SCLC model. (c) XPS spectra for the SnO_2 and PVP-SnO_2 films deposited on ITO substrates. The inset gives the XPS spectra of Sn $3d_{5/2}$ and Sn $3d_{3/2}$ of the SnO_2 and PVP-SnO_2 films. (d) Schematic images of the SnO_2 and PVP-SnO_2 films.

The study of the perovskite film quality, including the grain size, crystallinity, surface coverage, *etc.*, is very important for high-performance perovskite solar cells. Top-view SEM was used to study the surface morphology of perovskite films deposited on different ETLs, which is provided in Fig. 3c and d. It is apparent from these images that continuous pinhole-free films were obtained, which indicates films with full surface coverage. The crystal grain sizes of the perovskite film on PVP-SnO_2 are more uniform and larger than those of the perovskite film deposited on SnO_2. Moreover, the perovskite films deposited on both SnO_2 and PVP-SnO_2 have a white phase, which was confirmed to be PbI_2.[43] PVP can help the growth of the SnO_2 layer, thus improving the morphology of the perovskite layer. As the SEM shows, the crystal grain size of the perovskite based on PVP-SnO_2 is larger than that on SnO_2, which can reduce the carrier recombination between the grain boundaries of the perovskite. As a result, the reverse saturation current is decreased and the open circuit voltage is increased. As we know, the growth of a perovskite is highly dependent on the substrate, and especially depends on the wetting properties of the substrate.[44] The different growth behavior of SnO_2 and PVP-SnO_2 could be explained by two possible reasons: the different hydrophilic properties between SnO_2 and PVP-SnO_2 could be one reason; when the perovskite precursor was spin coated on the SnO_2 layer, it wetted very well with SnO_2 and nucleated everywhere due to the highly hydrophilic properties of SnO_2, while the perovskite could only nucleate on some places of the PVP-SnO_2 surface due to inferior hydrophilic properties compared with SnO_2. On the other hand, the PVP-SnO_2 film is dense and consists of particles; the PVP-SnO_2 particles could provide effective nucleation sites to initiate perovskite crystal growth. Both of these could lead to larger perovskite crystals on PVP-SnO_2 than on the SnO_2 layer. As a result, the larger perovskite crystal grains are beneficial for electron transfer and then improve the photoelectric performance. The perovskite film on PVP-SnO_2 has less PbI_2 phase than the perovskite film on SnO_2. According to the literature,[45,46] an appropriate PbI_2 amount is beneficial to the performance of PSCs.

XRD analysis of perovskite films deposited on different ETLs is also performed. The XRD patterns of the perovskite films spin-coated on the ITO/SnO_2 and ITO/PVP-SnO_2 substrates are shown in Fig. 4a. It is found that the perovskite film on PVP-SnO_2 has almost the same diffraction peaks as the perovskite on the pure SnO_2. A typical perovskite peak was found in perovskite films deposited on both ITO/SnO_2 and ITO/PVP-SnO_2 at 14.2°. At the same time, a peak at 12.7° corresponding to PbI_2 was observed, which has a negative impact on the performance of perovskite solar cells. The perovskite on PVP-SnO_2 has less PbI_2 than the perovskite on SnO_2, which is consistent with the conclusion of SEM in Fig. 3c and d.

Photoluminescence (PL) spectra and time-resolved photoluminescence (TRPL) spectra can be used to effectively analyze the interface charge transfer of PSCs. As shown in Fig. 4b, the PL spectra of the perovskites on ITO, SnO_2 and PVP-SnO_2 were measured to evaluate the interface charge transfer between the perovskite and the ETL. It can be clearly found that the PL peaks of the perovskite film spin-coated on ITO, ITO/SnO_2 and ITO/PVP-SnO_2 at 780 nm were quenched effectively when the SnO_2 or PVP-SnO_2 ETL was used, which demonstrated that the SnO_2 ETL can help the electron extraction from the perovskite to the electrode. The perovskite on PVP-SnO_2 exhibits more quenched PL than on SnO_2, which is related to the more efficient electron transfer from the perovskite to the ETL. The results of TRPL show that the lifetime of the perovskite layer was significantly reduced when it was deposited on PVP-SnO_2 compared to the one on SnO_2, which indicates that efficient electron transfer occurred from the perovskite to PVP-SnO_2 as shown in Fig. 4c. From all of the above analyses, we conclude that PVP-SnO_2 as the ETL might improve the performance of perovskite solar cells.

We have proven that the performance of the device is improved by adding a small amount of PVP to the SnO_2 solution. To confirm the positive effect of the PVP doping on the photovoltaic performance of PSCs, the performance of the devices based on SnO_2 and PVP-SnO_2 (3 mg mL^{-1} PVP) with the same device structure was compared, and the corresponding results are shown in Fig. 5a. For the PVP-SnO_2 device, the best device shows an efficiency of 19.55% with V_{OC} = 1.120 V, J_{SC} = 23.83 mA cm^{-2} and FF = 73.27%. The highest efficiency of the device without the PVP additive is only 17.50%.

Fig. 5b shows the external quantum efficiency (EQE) spectra and the corresponding integrated currents of the PSCs with different ETLs. The devices exhibit a broad peak above 80% in

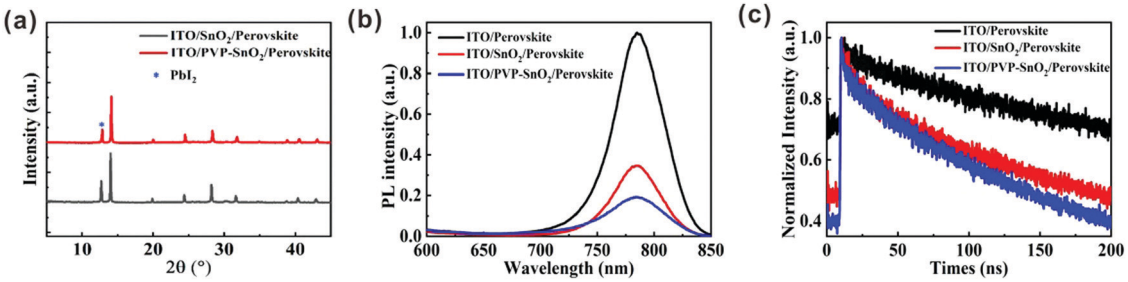

Fig. 4 (a) X-ray diffraction (XRD) patterns of the perovskites deposited on different ETLs. (b) Photoluminescence (PL) spectra of the perovskite films deposited on ITO, SnO_2 and PVP-SnO_2 substrates. (c) Normalized time-resolved photoluminescence (TRPL) spectra of the perovskite films deposited on ITO, SnO_2 and PVP-SnO_2 substrates.

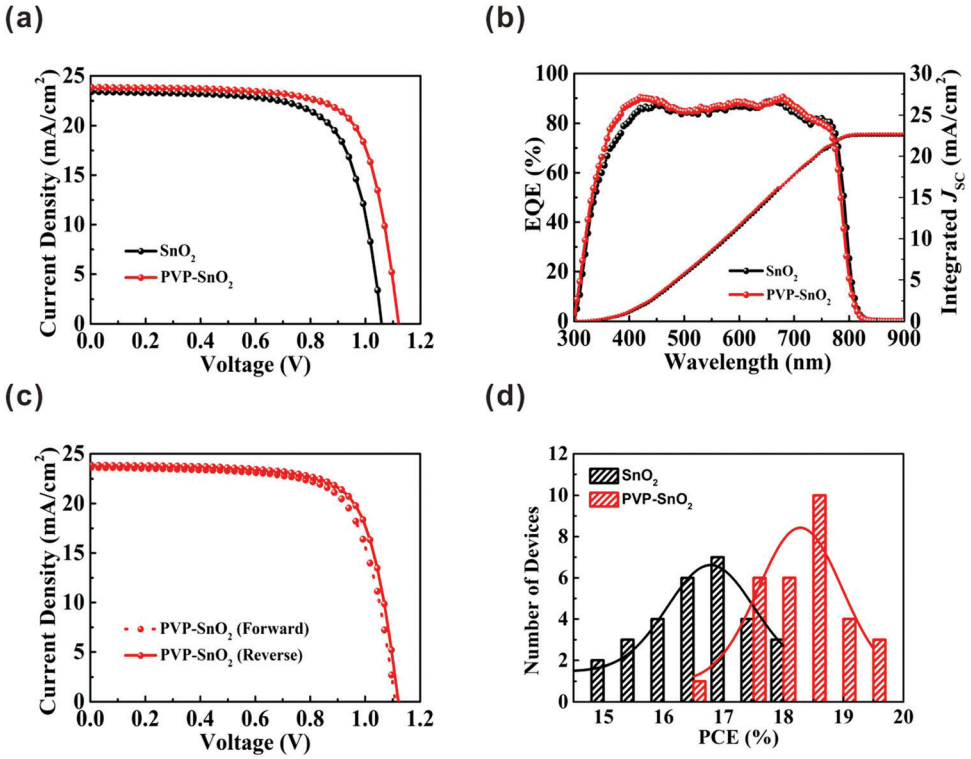

Fig. 5 (a) J–V curves of the best-performing perovskite solar cells using the SnO_2 and PVP-SnO_2 ETLs measured under reverse scans. (b) The external quantum efficiency (EQE) spectra and the corresponding integrated J_{SC} curves for the best-performance PSCs with different ETLs. (c) J–V curves of devices using the PVP-SnO_2 ETL under reverse and forward scans. (d) The PCE distribution histogram of the planar type PSCs with different ETLs.

Table 2 Photovoltaic performance of perovskite solar cells based on SnO_2 and PVP-SnO_2 with forward and reverse scans

ETLs	Scanning direction	V_{OC} (V)	J_{SC} (mA cm^{-2})	FF (%)	PCE (%)	Average PCE (%)
SnO_2	Forward scan	1.045	23.41	68.19	16.68	16.21 ± 3.03
	Reverse scan	1.057	23.39	70.75	17.50	
PVP-SnO_2 (3 mg mL^{-1})	Forward scan	1.109	23.61	71.59	18.76	17.74 ± 3.01
	Reverse scan	1.120	23.83	73.27	19.55	

the range of 400 to 760 nm. The integrated current values calculated from the EQE spectra are 22.55 and 22.67 mA cm^{-2} for the devices with SnO_2 and PVP-SnO_2 as the ETL, respectively, which are close to the J–V measurements (within the error range). For the hysteresis test,[47] Fig. 5c shows the J–V curves of devices using the PVP-SnO_2 ETL under reverse and forward scans. The PVP-SnO_2-based device yielded a PCE of 19.55% from a reverse current–voltage scan, with V_{OC} = 1.120 V, J_{SC} = 23.83 mA cm^{-2} and FF = 73.27%. A small amount of hysteresis was observed with a forward scan yielding PCE = 18.76%. The detailed parameters of the reverse scan and forward scan of the two devices with the pure SnO_2 and the optimized PVP-SnO_2 are summarized in Table 2. The results show that the PVP-SnO_2-based device has reduced hysteresis in comparison with the control device with SnO_2.

Fig. 5d shows the PCE distribution histogram for devices with different ETLs. It is apparent that the devices with the PVP-SnO_2 ETL show better repeatability and smaller standard deviations than those with the SnO_2 ETL. This result indicates that PVP-SnO_2 can be used as a good candidate for the ETL in planar PSCs. Without any encapsulation, the long-term stability of the PSCs with SnO_2 and PVP-SnO_2 was investigated in a nitrogen environment. The shelf-stability of PSCs with different ETLs as a function of storage time is shown in Fig. 6. The device with the PVP-SnO_2 ETL retains 88% of its initial PCE after 41 days of storage, while the device with the SnO_2 ETL dropped to 80% of its initial PCE after 41 days. It indicates that the device with the PVP-SnO_2 ETL is more stable than that with the SnO_2 ETL, which is ascribed to the improved contact between the perovskite and the PVP-SnO_2 ETL. It is known that the instability of perovskite solar cells is related to the degradation of the perovskite layer and the charge carrier transport layer. Because of the improved contact between the PVP-SnO_2 ETL and the perovskite layer, the PVP-SnO_2 based devices are more stable than the SnO_2 based devices.

Conclusion

In summary, the incorporation of PVP into SnO_2 improves the performance of planar perovskite solar cells. The characterization

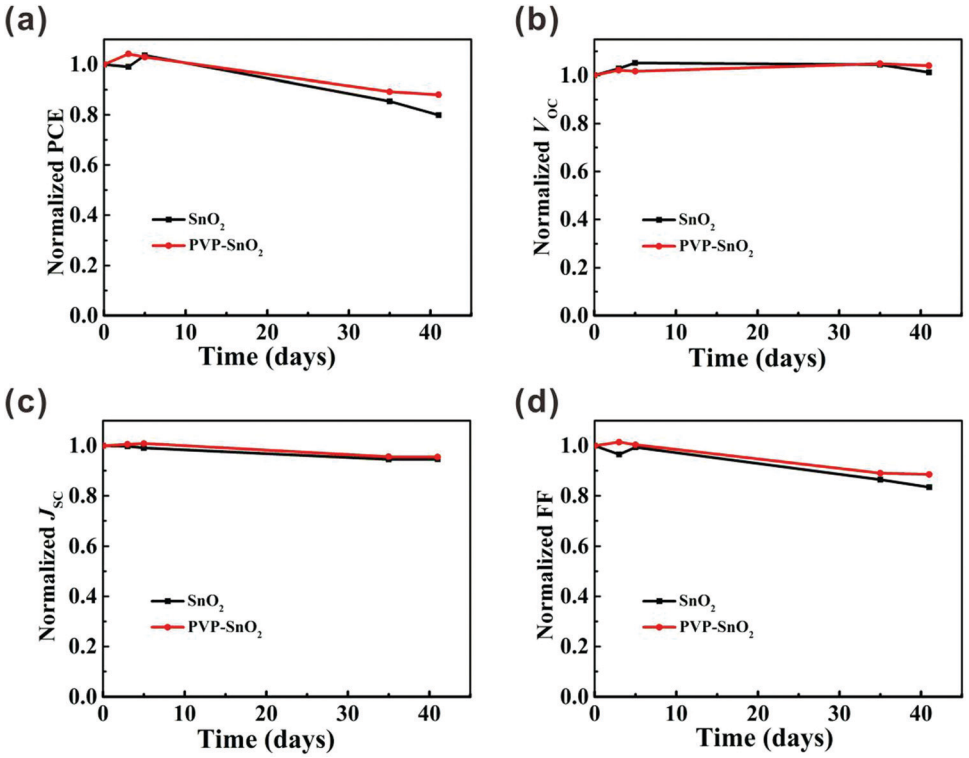

Fig. 6 The shelf-stability of perovskite solar cells in a glove box without any encapsulation. Normalized (a) PCE, (b) V_{OC}, (c) J_{SC} and (d) FF.

and analysis show that the PVP-SnO_2 ETL promotes electron collection and transfer, which inhibits charge accumulation at the interface between the ETL and the perovskite, resulting in a high efficiency. In addition the crystal grain sizes of the perovskite film on PVP-SnO_2 are more uniform and larger than the perovskite film deposited on SnO_2. As an result, the PCE of the planar PSCs has increased to 19.55% from with the baseline of 17.50% from the control PSC with the SnO_2 ETL, and the *J*–*V* hysteresis is alleviated. Therefore, we conclude that SnO_2 with a suitable PVP content is a promising electron transport material for high-performance PSCs, and provides a viable method for improving the performance of perovskite solar cells.

Experimental section

Materials

FAI, MABr, MACl, and spiro-OMeTAD were purchased from Xi'an Polymer Light Technology Corp. PbI_2 was purchased from Sigma-Aldrich Company. The SnO_2 colloid precursor was obtained from Alfa Aesar (tin(IV) oxide, 15% in H_2O colloidal dispersion). Polyvinylpyrrolidone (PVP) was purchased from Shanghai Aladdin.

Solar cell fabrication

ITO patterned glass substrates (1.5 cm × 1.5 cm) were ultrasonically cleaned by using detergent solution, deionized water, propanol and isopropanol for 15 minutes in each step. The ITO glass substrates were further cleaned by an ultraviolet ozone treatment for 20 minutes before depositing the ETL. In the process of preparing the device, two ETL solutions are mainly used, namely the SnO_2 precursor solution and the PVP-SnO_2 precursor solution. The SnO_2 precursor solution was obtained by mixing 1 mL of the aqueous SnO_2 solution with 3 mL of H_2O. For the PVP-SnO_2 precursor solution, first 1 mL of aqueous SnO_2 solution was mixed with 3 mL of water, and then PVP (2–5 mg mL^{-1}) was added to the SnO_2 solution. The SnO_2 and PVP-SnO_2 precursors were stirred at room temperature for five hours. The different ETLs were deposited onto the treated ITO glass substrate by spin-coating at 4000 rpm for 40 s, and the samples were immediately annealed on a hotplate at 180 °C for 20 min. The preparation of the different ETLs is carried out in air. After cooling, the substrates were subjected to UV ozone treatment for 15 min, and transferred into a glove box for the deposition of the perovskite layer. The lead iodide solution was prepared as follows: 599.3 mg of PbI_2 was dissolved in a mixed solvent of 1 mL of dimethylformamide (DMF) and anhydrous dimethyl sulfoxide (DMSO) at a temperature of 70 °C for one hour, wherein the volume ratio of DMF to DMSO was 9 : 1. The mixture solution was synthesized by dissolving FAI (60 mg), MABr (60 mg) and MACl (6 mg) in 1 mL isopropanol and stirred for one hour. The perovskite films were deposited using a two-step spin coating method. First, the PbI_2 solution was deposited onto different ETLs by spin-coating at 1500 rpm for 30 s, and then the substrates were annealed at 70 °C for 7 s to form PbI_2 films. After spin-coating with the mixed solution, the substrates were annealed at 135 °C for 15 min to form a dark perovskite layer in air. After deposition of the perovskite layer,

the substrates were transferred from the air to the glove box for the deposition of the HTL. The spiro-OMeTAD precursor solution was prepared by dissolving 72.3 mg spiro-OMeTAD, 35 μL of bis (trifluoromethane) sulfonimide lithium salt in acetonitrile (260 mg mL^{-1}) and 30 μL of *tert*-butylpyridine in 1 mL chlorobenzene. The spiro-OMeTAD precursor solution was subsequently coated on the top of the perovskite film at 2500 rpm for 30 s. Note that after spin-coating the spiro-OMeTAD layer, the substrates were placed in air in a humidity-control box for 12 hours to ensure sufficient oxidation of the spiro-OMeTAD film. Finally, 7.5 nm of MoO_3 and 100 nm of Ag were deposited by thermal evaporation at a vacuum condition of 9×10^{-5} Torr. The effective area of the perovskite cells reported in this work is 1.8 mm × 4.8 mm (0.0864 cm^2).

Device characterization

The power conversion efficiencies of the perovskite solar cells were measured from current density–voltage (*J–V*) curves using a Keithley 2400 source under a simulated AM 1.5G spectrum with an intensity of 100 mW cm^{-2} (450 W Newport 94023A solar simulator). The devices were tested in an N_2 glove box with the reverse scan (1.2 → 0 V, step 0.02 V, delay time 30 ms) and the forward scan (0 → 1.2 V, step 0.02 V, delay time 30 ms). The scanning electron microscopy (SEM) images of the perovskite surfaces and the cross-sections of the devices were measured using an S-4800 SEM setup. The external quantum efficiency (EQE) was measured using an Oriel LPCE-66894 in air. The transmission spectra of the films were measured by using a UV/vis spectrophotometer (PerkinElmer, Lambda 365). X-ray diffraction analysis was performed with a Bruker D8 Advance diffractometer operated at 30 kV and 10 mA at 2θ in the range of 10–60°, step 0.02° and scan speed 2.3° min^{-1}.

Conflicts of interest

There are no conflicts to declare.

Acknowledgements

This work was supported by The National Key R&D Program of China (2018YFB1500102), Zhejiang Provincial Natural Science Foundation of China (LQ18F040002) and Zhejiang Provincial Key Laboratory (No. 2013E10022).

References

1 M. M. Lee, J. Teuscher, T. Miyasaka, T. N. Murakami and H. J. Snaith, *Science*, 2012, **338**, 643.
2 P. Luo, Z. Liu, W. Xia, C. Yuan, J. Cheng and Y. Lu, *ACS Appl. Mater. Interfaces*, 2015, **7**, 2708.
3 F. Zhang, X. Yang, H. Wang, M. Cheng, J. Zhao and L. Sun, *ACS Appl. Mater. Interfaces*, 2014, **6**, 16140.
4 J. Burschka, N. Pellet, S. J. Moon, R. Humphry-Baker, P. Gao, M. K. Nazeeruddin and M. Grätzel, *Nature*, 2013, **499**, 316.
5 H. Zhang, J. Cheng, D. Li, F. Lin, J. Mao, C. Liang, A. K. Y. Jen, M. Grätzel and W. C. Choy, *Adv. Mater.*, 2017, **29**, 1604695.
6 E. H. Jung, N. J. Jeon, E. Y. Park, C. S. Moon, T. J. Shin, T. Y. Yang, J. H. Noh and J. Seo, *Nature*, 2019, **567**, 511.
7 F. Fu, S. Pisoni, T. P. Weiss, T. Feurer, A. Wäckerlin, P. Fuchs, S. Nishiwaki, L. Zortea, A. N. Tiwari and S. Buecheler, *Adv. Sci.*, 2018, **5**, 1700675.
8 A. Kojima, K. Teshima, Y. Shirai and T. Miyasaka, *J. Am. Chem. Soc.*, 2009, **131**, 6050.
9 M. He, B. Li, X. Cui, B. Jiang, Y. He, Y. Chen, D. O'Neil, P. Szymanski, M. A. EI-Sayed, J. Huang and Z. Lin, *Nat. Commun.*, 2017, **8**, 16045.
10 J. Qi, H. Xiong, C. Hou, Q. Zhang, Y. Li and H. Wang, *Nanoscale*, 2020, **12**, 3646–3656.
11 J. Qi, L. Li, H. Xiong, A. C. Wang, C. Hou, Q. Zhang, Y. Li and H. Wang, *J. Mater. Chem. A*, 2019, **7**, 26154–26161.
12 J. Qi, H. Xiong, G. Wang, H. Xie, W. Jia, Q. Zhang, Y. Li and H. Wang, *J. Power Sources*, 2018, **376**, 46–54.
13 B. Wang, J. Iocozzia, M. Zhang, M. Ye, S. Yan, H. Jin, S. Wang, Z. Zou and Z. Lin, *Chem. Soc. Rev.*, 2019, **48**, 4854–4891.
14 H. Tsai, W. Nie, P. Cheruku, N. H. Mack, P. Xu, G. Gupta, A. D. Mohite and H. L. Wang, *Chem. Mater.*, 2015, **27**, 5570.
15 R. Singh, A. Giri, M. Pal, K. Thiyagarajan, J. Kwak, J. J. Lee, U. Jeong and K. Cho, *J. Mater. Chem. A*, 2019, **7**, 7151.
16 B. Wang, M. Zhang, X. Cui, Z. Wang, M. Rager, Y. Yang, Z. Zou, Z. L. Wang and Z. Lin, *Angew. Chem., Int. Ed.*, 2020, **59**, 1611–1618.
17 W. Hu, W. Zhou, X. Lei, P. Zhou, M. Zhang, T. Chen, H. Zeng, J. Zhu, S. Dai, S. Yang and S. Yang, *Adv. Mater.*, 2019, **31**, 1806095.
18 B. Wang, J. Iocozzia, M. Zhang, M. Ye, S. Yan, H. Jin, S. Wang, Z. Zou and Z. Lin, *Chem. Soc. Rev.*, 2019, **48**, 4854–4891.
19 K. Domanski, E. A. Alharbi, A. Hagfeldt, M. Grätzel and W. Tress, *Nat. Energy*, 2018, **3**, 61.
20 H. J. Snaith, A. Abate, J. M. Ball, G. E. Eperon, T. Leijtens, N. K. Noel, S. D. Stranks, J. T. Wang, K. Wojciechowski and W. Zhang, *J. Phys. Chem. Lett.*, 2014, **5**, 1511.
21 J. Wei, H. Li, Y. Zhao, W. Zhou, R. Fu, Y. L. Wang, D. Yu and Q. Zhao, *Nano Energy*, 2016, **26**, 139.
22 J. Cao, B. Wu, R. Chen, Y. Wu, Y. Hui, B. W. Mao and N. Zheng, *Adv. Mater.*, 2018, **30**, 1705596.
23 Y. C. Wang, X. Li, L. Zhu, X. Liu, W. Zhang and J. Fang, *Adv. Energy Mater.*, 2017, **7**, 1701144.
24 P. Zhang, J. Wu, T. Zhang, Y. Wang, D. Liu, H. Chen, L. Ji, C. Liu, W. Ahmad, Z. D. Chen and S. Li, *Adv. Mater.*, 2018, **30**, 1703737.
25 W. Ke, G. Fang, Q. Liu, L. Xiong, P. Qin, H. Tao, J. Wang, H. Lei, B. Li, J. Wan, G. Yang and Y. Yang, *J. Am. Chem. Soc.*, 2015, **137**, 6730.
26 T. Bu, J. Li, F. Zheng, W. Chen, X. Wen, Z. Ku, Y. Peng, J. Zhong, Y. B. Cheng and F. Huang, *Nat. Commun.*, 2018, **9**, 4609.
27 Q. Jiang, L. Zhang, H. Wang, X. Yang, J. Meng, H. Liu, Z. Yin, J. Wu, X. Zhang and J. You, *Nat. Energy*, 2016, **2**, 1.
28 W. Ke, G. Fang, Q. Liu, L. Xiong, P. Qin, H. Tao, J. Wang, H. Lei, B. Li, J. Wan, G. Yang and Y. Yan, *J. Am. Chem. Soc.*, 2015, **137**, 6730.

29 Y. Huang, S. Li, C. Wu, S. Wang, C. Wang and R. Ma, *Chem. Phys. Lett.*, 2020, 137220.
30 W. Zhang, Y. Li, X. Liu, D. Tang, X. Li and X. Yuan, *Chem. Eng. J.*, 2020, **379**, 122298.
31 Z. Zhu, Y. Bai, X. Liu, C. C. Chueh, S. Yang and A. K. Y. Jen, *Adv. Mater.*, 2016, **28**, 6478.
32 W. Q. Wu, D. Chen, Y. B. Cheng and R. A. Caruso, *Sol. RRL*, 2017, **1**, 1700117.
33 S. Jeong, S. Seo, H. Park and H. Shin, *Chem. Commun.*, 2019, **55**, 2433.
34 J. Zhang, T. Zhang, L. Jiang, U. Bach and Y. B. Cheng, *ACS Energy Lett.*, 2018, **3**, 1677.
35 F. Qi, X. Deng, X. Wu, L. Huo, Y. Xiao, X. Lu, Z. Zhu and A. K. Y. Jen, *Adv. Energy Mater.*, 2019, **9**, 1902600.
36 D. Yang, R. Yang, K. Wang, C. Wu, X. Zhu, J. Feng, X. Ren, G. Fang, S. Priya and S. F. Liu, *Nat. Commun.*, 2018, **9**, 3239.
37 J. Wei, F. Guo, X. Wang, K. Xu, M. Lei, Y. Liang, Y. Zhao and D. Xu, *Adv. Mater.*, 2018, **30**, 1805153.
38 C. E. Small, S. Chen, J. Subbiah, C. M. Amb, S. W. Tsang, T. H. Lai, J. R. Reynolds and F. So, *Nat. Photonics*, 2012, **6**, 115–120.
39 L. La Notte, P. Cataldi, L. Ceseracciu, I. S. Bayer, A. Athanassiou, S. Marras, E. Villari, F. Brunetti and A. Reale, *Mater. Today Energy*, 2018, **7**, 105.
40 Z. Ma, Z. Tang, E. Wang, M. R. Andersson, O. Inganäs and F. Zhang, *J. Phys. Chem. C*, 2012, **116**, 24462.
41 Q. Liu, X. Zhang, C. Li, H. Lu, Z. Weng, Y. Pan, W. Chen, X. C. Hang, Z. Sun and Y. Zhan, *Appl. Phys. Lett.*, 2019, **115**, 143903.
42 R. Ranjan, A. Prakash, A. Singh, A. Singh, A. Garg and R. K. Gupta, *J. Mater. Chem. A*, 2018, **6**, 1037.
43 Q. Jiang, Z. Chu, P. Wang, X. Yang, H. Liu, Y. Wang, Z. Yin, J. Wu, X. Zhang and J. You, *Adv. Mater.*, 2017, **29**, 1703852.
44 C. Bi, Q. Wang, Y. Shao, Y. Yuan, Z. Xiao and J. Huang, *Nat. Commun.*, 2015, **6**, 7747.
45 Y. C. Kim, N. J. Jeon, J. H. Noh, W. S. Yang, J. Seo, J. S. Yun, A. Ho-Baillie, S. Huang, M. A. Green, J. Seidel, T. K. Ahn and S. I. Seok, *Adv. Energy Mater.*, 2015, **6**, 1502104.
46 B. Shi, X. Yao, F. Hou, S. Guo, Y. Li, C. Wei, Y. Ding, Y. Li, Y. Zhao and X. Zhang, *J. Phys. Chem. C*, 2018, **122**, 21269–21276.
47 P. Liu, W. Wang, S. Liu, H. Yang and Z. Shao, *Adv. Energy Mater.*, 2019, **9**, 1803017.